



Superior functionality of niobium pentoxide nano-rod/tripod photocatalyst synthesized using polyethyleneimine as a soft template for the abatement of methylene blue under UV and visible irradiation

Neha Kumari^{1,2} · Sanjoy Kumar Samdarshi^{1,2} · Ranjana Verma³ · Kumar Gaurav^{1,2} · Arnab S. Bhattacharyya^{2,4} · Kaustubha Mohanty⁵ · Uday Deshpande⁶

Received: 25 May 2023 / Accepted: 6 November 2023 / Published online: 16 November 2023
© The Author(s), under exclusive licence to Springer-Verlag GmbH Germany, part of Springer Nature 2023

Abstract

Polyethyleneimine (PEI) capping agent-cum-template-mediated synthesis of niobium oxide nanoparticles is reported to explore its impact on the resultant morphology, porosity, crystallinity, phase complexation, and thus on the photocatalytic activity. The resultant niobium oxides calcined at 800°C and 1000°C crystallized into highly ordered nano-rod/tripod nanostructure with inter-rod angle <math><120^\circ</math> having orthorhombic phase and heavily agglomerated rod-like nanostructures having monoclinic crystal phase, respectively. Contrary to the expectations, the nano-rod/tripods showed superior photocatalytic degradation kinetics and high adsorption of methylene blue dye in the hydrocolloid than formerly reported monoclinic nanoparticles. The best adsorption capability and photocatalytic activity are observed for the sample calcined at 800°C, resulting in a combined degradation efficiency of 98.8% of methylene blue dye. The adsorption characteristics, stability of the hydrocolloid system, the existence of oxygen vacancies, and the distinct morphology of the photocatalytic nano-rod/tripods are mainly responsible for this behavior. The process and the performance of unique nanostructure over others presents a superior alternative.

Keywords Niobium pentoxide · Soft template · Photocatalyst · Nano-rod/tripods · Methylene blue · Oxygen vacancies

Introduction

Heterogeneous photocatalysis using solar irradiance is among the most attractive avenues for environmental rectification, carbon valorization, and green fuel hydrogen production (Prado et al. 2008; Prieto-Mahaney et al. 2009; Zhu et al. 2013; Karimi-Maleh et al. 2023; Liu et al. 2015). Photocatalyst materials based on transition metal oxides such as niobium have generated interest as a promising option owing to the possibility of tunability of its band gap; complexation of its phases; and hetero- or homo-compositization with other oxides or its other oxidation states, respectively (Tsang et al. 2012; Ebrahimi et al. 2021; Zhang et al. 2014; Mohammadi et al. 2020; Wang et al. 2018). Nb_2O_5 , being thermodynamically more stable than other oxides of niobium, finds a number of applications in sensors, energy storage, and electro-chromic devices in addition to photocatalysis (Abreu et al. 2021; Kulkarni et al. 2017; Lee et al. 2002; Liu et al. 2015; Prado et al. 2008; Zhang et al. 2014; Zhao et al. 2016). Here, the option of developing and modifying the morphologies along with the electronic structure offers the possibility of tuning

Responsible Editor: Sami Rtimi

✉ Sanjoy Kumar Samdarshi
drksamdarshi@gmail.com

- ¹ Centre of Excellence in Green and Efficient Energy Technology, Central University of Jharkhand, Ranchi, Jharkhand 835205, India
- ² Department of Energy Engineering, Central University of Jharkhand, Ranchi, Jharkhand 835205, India
- ³ Department of Physics, Institute of Sciences, Banaras Hindu University, Varanasi, Uttar Pradesh 221005, India
- ⁴ Department of Nanotechnology, Central University of Jharkhand, Ranchi, Jharkhand 835205, India
- ⁵ Department of Chemical Engineering, Indian Institute of Technology, Guwahati, Assam 781039, India
- ⁶ University Grant Commission Department of Atomic Energy, Consortium for Scientific Research (UGC-DAE CSR), Indore, Madhya Pradesh 452001, India

its physical and chemical properties for desired applications (Taghavi et al. 2022). A variety of precisely controlled 1D and 2D nanostructures, such as nanoparticles, nanorods, nanowires, and nanobelts, have been synthesized over recent years (Cui et al. 2021; Hayati et al. 2021; Jian et al. 2019; Zhao et al. 2016). However, for meticulous command over morphology and size, the method of synthesis remains a critical step. Among the various methods, the template-based synthesis represents a successful process to modulate nanoparticle interaction through the surface (Pérez-page et al. 2016; Phan and Nguyen 2017; Poolakkandy and Menampambath 2020; Xie et al. 2016). Utilizing a solid substrate or a solution technique for templating is a technology that influences the morphology by restricting the crystal nucleation and development during the initial construction. It is followed, finally, by template removal using various physical or chemical methods such as heat treatment or sintering, lithographing or etching, dissolution, etc., to get the desired system (Pérez-page et al. 2016; Xie et al. 2016). Recently conducting polymers such as polyaniline, polyphenylenediamine, polyetheramide, and their derivatives have found excellent utility as promising templates for the synthesis and design of photocatalysts (Essawy et al. 2017; Watanabe et al. 2021; Zhang et al. 2014). Polyethyleneimine (PEI), consisting of two carbon chains and an amine group in a repeating unit, is a polymer cationic in nature. The amine functional group serves as a ligand for nanoparticle attachment, and its hyperbranched structure prevents the agglomeration of nanoparticles. PEI exhibits an additional intriguing capability when employed as a modifier. It can effectively reduce the work function of materials it comes into contact with. A lowered work function can enhance the ease with which electrons are transported across interfaces, leading to an improved charge transfer process (Alavi et al. 2015; Jain et al. 2020; Li et al. 2014; Martín et al. 2021; Zhang et al. 2014).

A simple PEI-assisted hydrothermal method for synthesizing niobium pentoxide has been reported here using niobium oxalate, a low-cost precursor (S1). For the first time, niobium oxide nanorods oriented in tripod-like structures (nanorod/tripod) have been synthesized with PEI as the structure director. This niobium pentoxide nanorod/tripod of the orthorhombic phase, formed after calcination at 800°C, shows superior kinetics in dye degradation compared to nanorods of the monoclinic phase, formed at a calcination temperature of 1000°C. As reported earlier, the niobium pentoxide without the polymer template showed maximum dye degradation kinetics with the monoclinic phase of the sample formed after calcination at 1000°C (Kumari et al. 2020). This low-temperature synthesis is desirable as it not only reduces the energy intensity but also the carbon emission and the risks of high temperature. Also, the sample is beautifully grown nanorod/tripod-ordered nanostructures with

superior functionalities. Here, methylene blue dye has been used as a probe pollutant to examine the photoactivity of the niobium pentoxide catalyst having diverse real-world applications in wastewater treatment (Ancy et al. 2022; Arcanjo et al. 2018; Rueda-Marquez et al. 2020; Souza et al. 2016), hydrogen production, and CO₂ valorization.

Experimental details

Synthesis of niobium pentoxide using PEI as soft template

Typically, 2.26g of ammonium niobium oxalate hydrate (ANO) was blended in 40 ml of distilled water in a beaker. In addition, 40 ml of DI water was combined with 0.4 g of branched PEI and swirled for 30 min. One milliliter of 2M HNO₃ soln. was added to a beaker containing polymer, and then the polymer mixture was poured into the ANO solution. The mixture was then poured into a teflon-lined autoclave and treated in a muffle furnace at 200°C for 24 h. The precipitate obtained was washed thoroughly with ethyl alcohol and double distilled water, dried, and calcined at 800° and 1000°C, respectively. The samples thus obtained are, henceforth, referred to as pN80 and pN100, respectively. The purity and make of the precursor used are mentioned in the Section 1 of the Supplementary File.

Characterization essays

Phase and crystallite size were determined by X-ray diffraction using Proto AXRD Benchtop, Canada, with Cu target. Morphology and structure were studied using FESEM, Model: Nova Nano FESEM 450 (FEI, USA) equipped with EDX attachment. The UV–Visible–NIR spectrophotometer Lambda 19 Perkin Elmer, USA, was used for evaluating the spectral response. Photoluminescence (PL) spectrum was recorded using Fluoromax-4, Horiba Scientific, USA, to identify the trap states with excitation at 350 nm. X-ray photoelectron spectroscopy (XPS) measurements were carried out using X-ray photoelectron spectroscope (SPECS, Germany) using Al K α radiation by applying 13 kV anode voltage. The Talos F200i S/TEM (HRTEM-200KV) system, Thermo Fisher Scientific, USA, was used to obtain FEG-transmission electron microscope (HRTEM) images. The BET analyzer, NOVA touch LX Quantachrome system, Austria, was used for determining pore size. The Litesizer 500, Anton Paar, Austria, particle analyzer was used to measure the electro kinetic potential of the colloidal solution.

Photocatalysis test

Photodegradation of the catalysts was estimated by examining the degradation kinetics of a probe pollutant (methylene blue (MB)) in UV illumination using Philips TUV 15W/G15T8 and visible radiation using Murphy IP65 20W LED white light, respectively, in a photoreactor with the average temperature maintained at 35°C in a batch type reactor. The degradation kinetics was evaluated using the catalyst loading of 0.5 g/l under identical ambient conditions. The volume of the pollutant sample was taken to be 30 ml, and the concentration of the pollutant in 30 ml was 4.25 ppm. The intensity of the UV irradiance was measured as 0.15 Wm⁻², while the visible irradiance was measured as 14.5 Wm⁻² using a research radiometer from International Light, USA. For the UV irradiance, the main wavelength of the source was 257.3 nm. Similarly, for the visible irradiance, the main wavelength of the source was 426 nm. These wavelengths were positioned 29 cm away from the beaker mouth to ensure effective illumination of the reaction mixture. The distance between the light source and the catalyst surface was set at 35 cm. The adsorption-desorption equilibrium was obtained by keeping the colloidal solution under complete dark conditions for 2 h. This was followed by illuminating the system with UV/ visible light and collecting samples

in a centrifuge tube at 30-min intervals till 240 min and centrifuging them. The absorbance of the supernatant was checked at the wavelength of 664 nm (corresponding to the absorption maxima of methylene blue) using a UV–visible spectrophotometer (Shimadzu UV 3600 Plus, Japan).

Adsorption analysis

A careful adsorption analysis was also carried out using adsorption kinetics and adsorption isotherm. Fifteen milligrams of each of the samples was dispersed in 30-ml methylene blue solution and kept in the dark at constant stirring at room temperature to study the adsorption mechanism. One milliliter of MB solution was collected at an interval of 30 min centrifuged and analyzed using UV VIS absorption spectra.

Results and discussion

Structural analysis

The synthesized samples were first subjected to XRD analysis to investigate their phase formation and crystallite size. As depicted in Fig. 1a, both the samples show crystalline

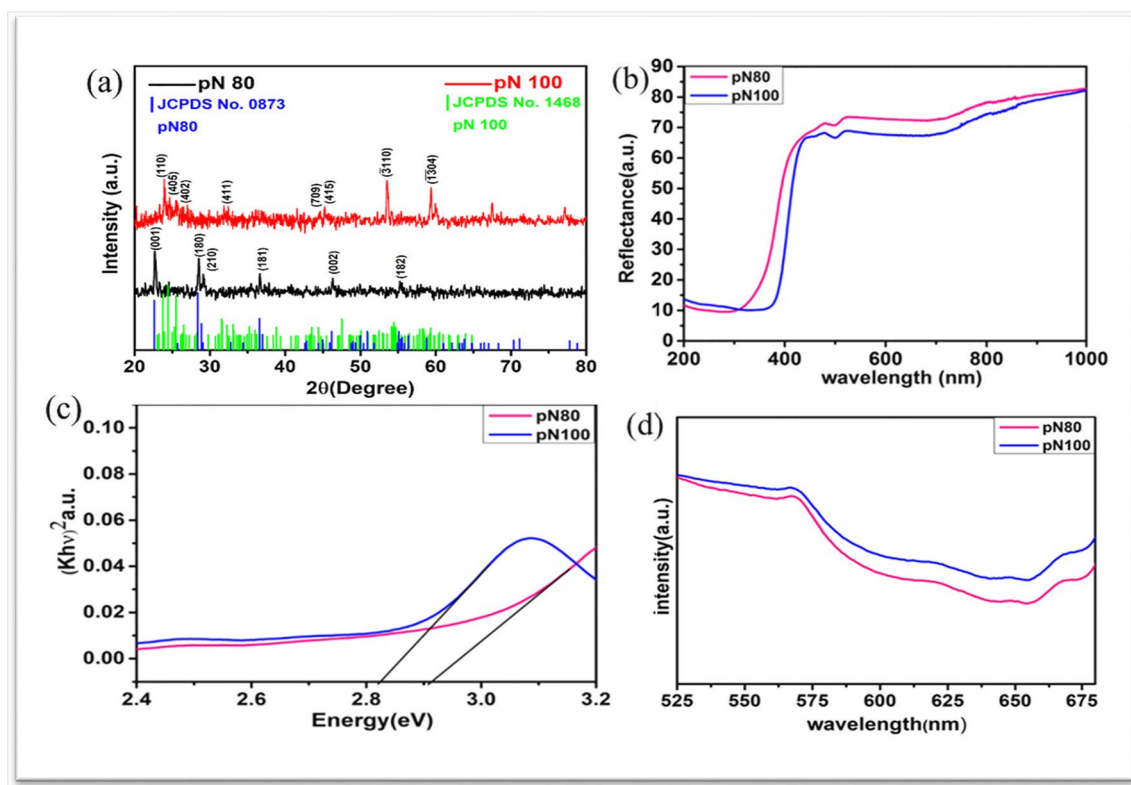


Fig. 1 a Powder XRD pattern for pN-80 and pN-100 samples. b UV–Vis diffuse reflectance spectra of pN80 and pN100 samples. c Kubelka–Munk transformed reflectance spectra having the band gap of the catalysts. d Photoluminescence spectra of pN80 and pN100 samples

structure with pN80 having orthorhombic phase (JCPDS No.00-030-0873) and pN100 a poorly developed crystalline monoclinic structure with a right shift in peak positions (JCPDS No. 00-037-1468) (Nowak and Ziolk 1999; Lin et al. 2011; Raba et al. 2016; Hu et al. 2020). The right shift can be attributed to the strained structure, which can be further explored in FESEM images. The crystallite size obtained using the Scherrer formula is mentioned in Table 1, and the cell constant in supplementary section S3 Table S.1. There is a decrease in crystallite size at higher temperatures, which may be due to structural distortion with associated phase transformation.

Morphological characterization

The morphology of samples pN80 and pN100 was analyzed using FESEM images, as shown in Fig. 2. The images confirm the formation of evenly distributed ordered nanorods

Table 1 Crystallite size, phase, and band gap of niobium oxide catalyst calcined at different temperatures

S.N.	Sample	Crystallite Size (nm)	Phase	Band gap (eV)
1	pN-80	20.11	Orthorhombic	2.91
2	pN-100	17.65	Monoclinic	2.84

arranged in the form of tripods, with inter nanorod angle being ~ 120 for pN80 samples as calculated using image J software. However, the particles of the high-temperature sample appear to be agglomerated. The niobium-to-oxygen ratios, as confirmed from the EDX spectrum (Fig. 2c, f (inset)), are 2:3 for pN80 and 2:5 for pN100 indicating pN80 to be an oxygen-deficient system while pN100 to be maintaining the stoichiometric ratio of Nb_2O_5 . At higher temperatures, annealing will restructure the crystals and reduce defects, and this is quite observed in the pN100 sample. In the case of the pN100 annealed sample, the samples undergo complete restructuring, forming the most stable phase of monoclinic Nb_2O_5 and involving the formation of Nb-O bonds attaining crystallinity. This result is also supported by the XPS studies. It also signifies that oxygen deficiency may also be caused by morphological changes. More images have been provided for better insight into morphology in section S4 Fig S1.

The TEM images and SAED pattern of pN-80 and pN-100 nanostructures are shown in Fig. 3a–f, respectively. The HRTEM images show spacing of 0.344nm for pN-80 lattice fringes (Fig. 3d) due to (041) (JCPDS code:00-030-0873) and 0.244nm for pN100 (Fig. 3f) due to (115) plane (JCPDS code: 00-037-1468). The samples appear to be polycrystalline in nature, as evident from the SAED pattern for pN-80 and pN-100 samples shown in Fig. 3 c and f (inset), respectively; the diffraction ring corresponding to

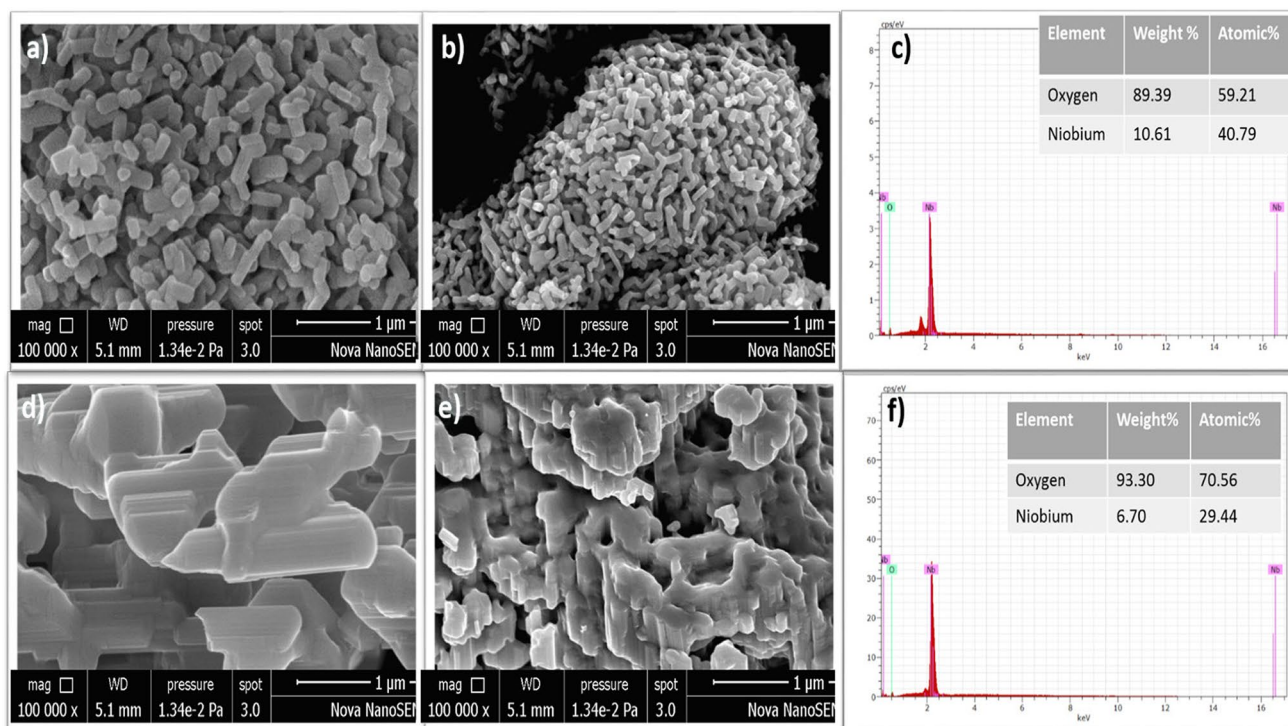


Fig. 2 FESEM micrographs of a–b pN-80 and d–e pN-100 and EDX with oxygen and niobium composition (inset) of c pN-80 and f pN-100

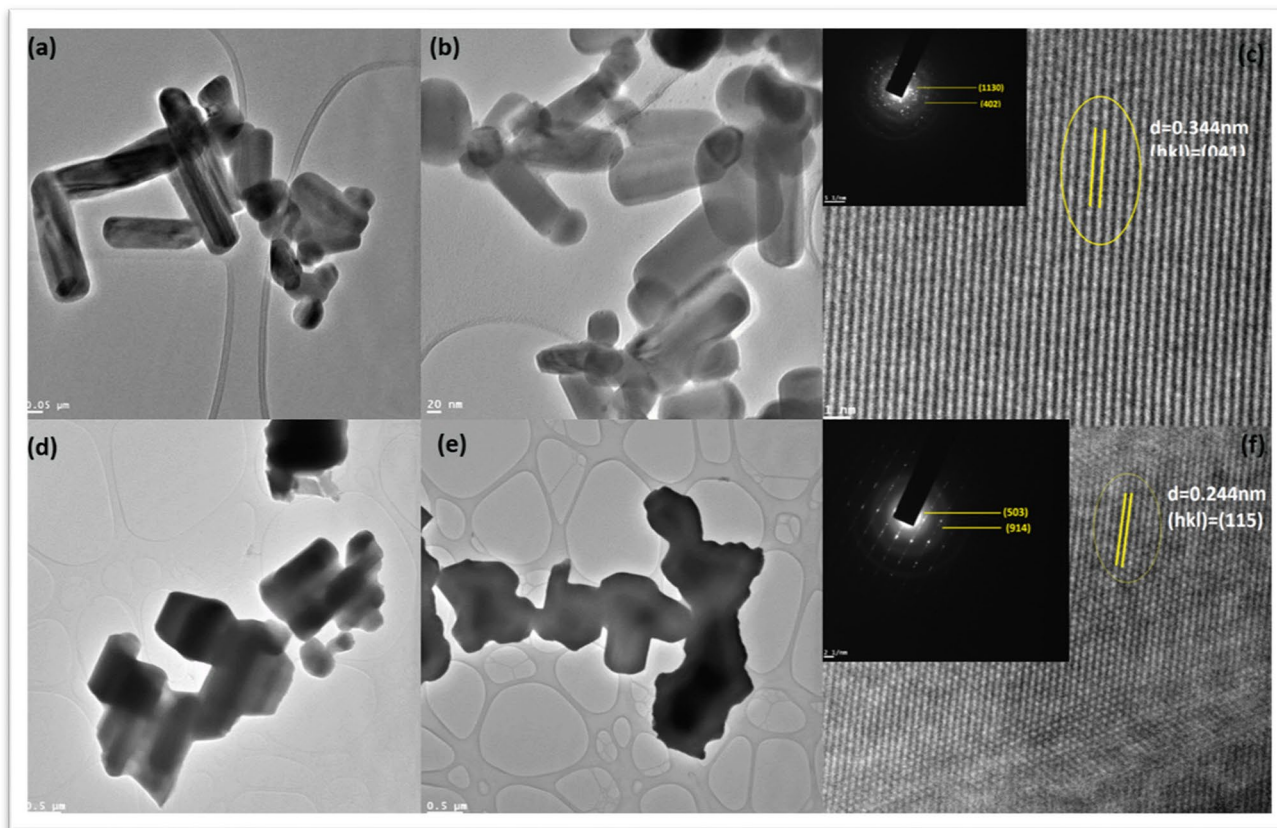


Fig. 3 HR-TEM images and SAED pattern for sample pN-80 (a–c) and pN-100 (d–f)

(1130), (402) and (503), (914) for pN80 and pN100, respectively, was determined using image J software (<https://wsr.imagej.net/distros/win/ij153-win-java8.zip>). The particle size was also analyzed using the software, as shown in S5 Fig S2, and plotting the histogram of the size distribution of the particle. The average size of the particle for pN80 is ~58.60 nm. The particle for pN100 appears to be too agglomerated for the determination of particle size using the software.

Optical characterization

The UV-VIS DRS reflectance spectral response is presented in Fig. 1b. For samples calcined at higher temperatures, the spectral response is found to be red-shifted. The optical band gap of the samples, determined by applying the Kubelka-Munk approach, as mentioned in section S6 equation S1, has been shown in Table 1 and Fig 1c. The potential reasons for the decrease in the band gap include phase change of the crystallite sample, distortion of the crystal lattice, and the resultant weakened interatomic bonds (Essawy et al. 2017). pN100 does not show any direct correlation with crystallite size and band gap in relation to pN80. This may be due to other factors which are explored further (Cui et al. 2021).

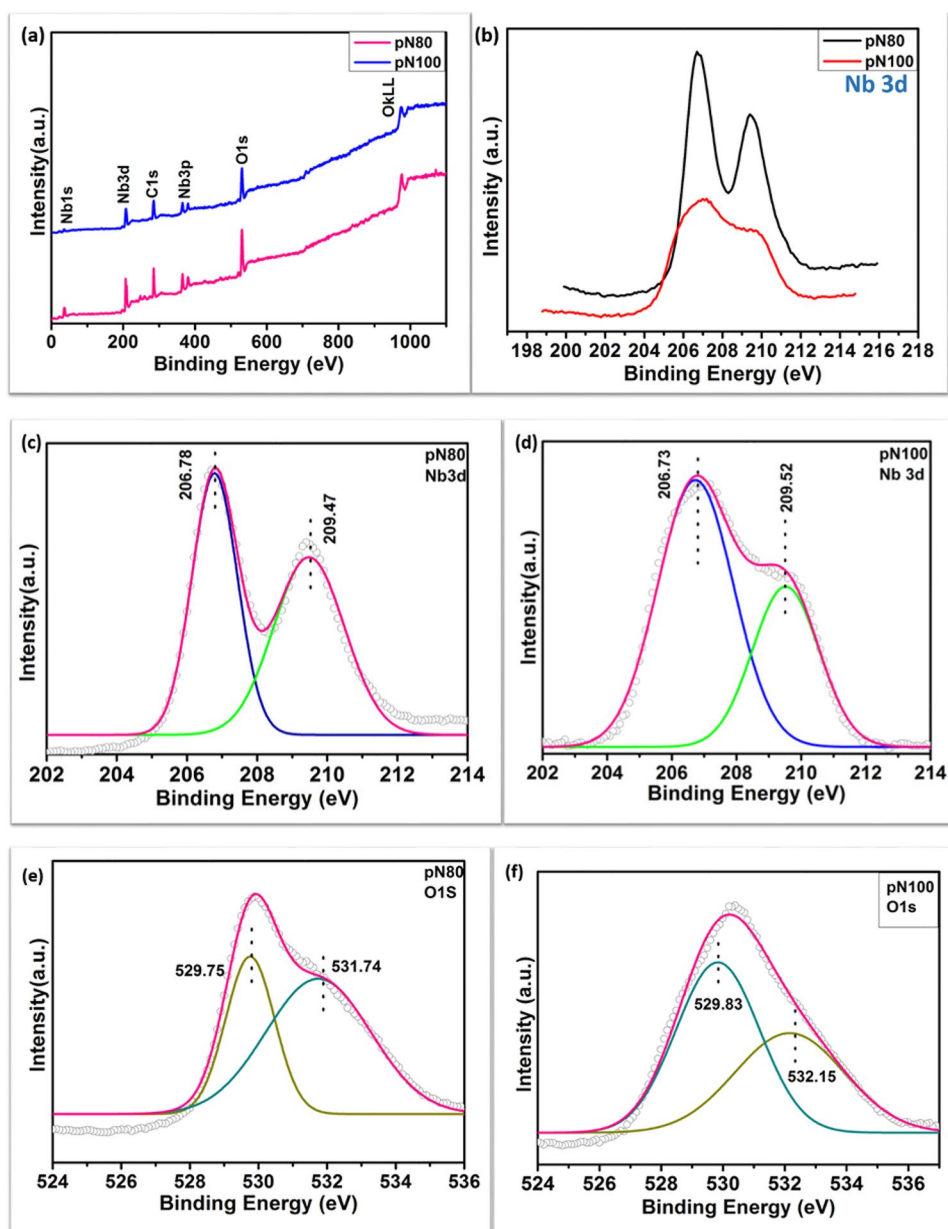
Figure 1d shows the trap states, vacancies, and intrinsic defects identified/studied using the PL spectra of the specimen excited at the wavelength of 350 nm (He et al. 2014). The significant emission peak in the range 525–650nm results from oxygen vacancies and surface defects, where the transition involves the energy levels within the band gap (Chen et al. 2017; Usha et al. 2015; Yan et al. 2014). There is no change in PL peaks in the pN100 sample calcined at high temperature; however, quenching of the PL intensity is more in the pN80 sample, which can be a result of oxygen vacancies and higher surface defects signifying lower recombination in pN80 sample (Kulkarni et al. 2017; Yan et al. 2014). The band gap estimated using PL was recorded to be 2.78 eV and 2.71 for the pN80 and the pN100 samples, respectively, which is less than that obtained from UV-vis reflectance spectrum analysis. This is ascribed to Nb₂O₅, which is an indirect band gap semiconductor that loses its energy through phonon emission as per Schokley Read Hall recombination in which the electron passes its energy to the phonons, or the traps present between conduction and valence band (Usha et al. 2015). So, the band edge emission spectra of PL may not correspond well with the band gap of indirect semiconductors.

XPS analysis

The XPS spectra were examined to study the chemical bonding of Nb in the samples. The existence of C, Nb, and O on the surface of the as-prepared samples is validated from the survey scan and is represented in Fig. 4a. The high-resolution XPS peaks of Nb 3d and O1s for both the samples are shown in Fig. 4c–f, and that of C1s is shown in figure S3. Nb 3d is comprised of doublets that represent the orbital splitting of $3d_{5/2}$ spins corresponding to binding energy 209.47eV, and $3d_{3/2}$ binding energy at 206.78eV for pN80; and 209.47eV and 206.78eV for pN100 as presented in Figs. 4c and 6d, respectively, agree well with the binding energy of oxidation state Nb⁵⁺ (Chen et al. 2019; Kong

et al. 2016). The oxidation state of the sample does not change with increasing temperature. The energy separation between the two peaks of pN80 and pN100 is 2.69 and 2.79 eV, respectively, which is equivalent to reported values (She et al. 2018; Singh et al. 2016). The FWHM of the niobium doublets increases with an increase in temperature due to distortion of structures resulting from agglomeration. The deconvoluted XPS spectrum of C 1s for pN80 has 4 peaks, as shown in Fig S3(i). The peaks at 284.58eV and 283.16eV are sp² and sp³ hybridized carbon, representing the surface of the adventitious carbon (Gupta et al. 2018). In Section S7 Fig S3(i), the peak observed at 286.4 and 288.1 is associated with hydroxyl and carbonyl groups, respectively (Kaciulis et al. 2014). In the pN100 sample, there is a shift in the peak

Fig. 4 XPS analysis of catalyst pN-80 and pN-100. **a** XPS survey scan of pN-80 and pN-100. **b** Nb 3d cumulative graph of both samples. **c** Nb 3d XPS spectra of pN80. **d** Nb 3d XPS spectra of pN-100. **e** Nb 3d XPS spectra of O 1s XPS spectra of pN-80 sample. **f** O 1s XPS spectra of pN-100



position while the peak at 286.4 disappears, as shown in figure S3(ii), which agrees well with the literature (Usha et al. 2015). The peaks of O1s in Fig. 4e and f at 529.75 eV and 529.83 eV are characteristic peaks representing anionic oxygen of Nb–O bond in Nb₂O₅ and surface oxygen, respectively (Dupin et al. 2000). The peaks in the range 531.6–532.15 eV, as shown in Fig. 4e and f, may be associated with hydroxyl/oxygen vacancies and adsorbed water group; however, the shift of peak towards lower binding energy, i.e., from 532.15 eV to 531 eV in the pN80 sample, is due to the creation of oxygen vacancies, also evident in PL and EDX results reported (Usha et al. 2015; Singh et al. 2016; Gupta et al. 2018; Merino et al. 2006; Ma et al. 2015).

BET analysis

N₂ adsorption-desorption isotherm was used to analyze the samples' textural characteristics, as illustrated in Fig. 5a and b. For the pN80 sample, the isotherm appears to be type II in nature, suggesting the samples to be microporous and type IV with hysteresis type H1 and an open loop for pN100 (Ma and Rosenberg 2001; Lee et al. 2002; Kulkarni et al. 2017; Lakhi et al. 2017). An open loop signifies uneven mesoporosity or narrow needle-shaped pores. This can be caused by the presence of sophisticated micropores or mesopores (Kumari et al. 2020). Specific surface area and pore volume decrease

with an increase in temperature, as in sample pN100, which is attributed to the development of irregularities in the particles with pores getting occupied and a consequent decrease in the surface area (Lee et al. 2002). The decrease in surface area may result from morphological transformation, as revealed in FESEM. Also, the hysteresis shape suggests agglomeration in the particles (Boruah et al. 2019). In the pN80 sample, the desorption curve with higher adsorption quantity than the adsorption curve is ascribed to the capillary condensation, provided the material is mesoporous in nature. This is confirmed by the nature of the isotherm; however, the negative value of volume indicates that the structure might have collapsed after extreme heating, leading to limited physisorption of the adsorbate. Perhaps this is the reason for the decrease in the photoactivity of the pN100 sample. The pore blockage or distortion of the morphology resulting from agglomeration, as suspected in the morphological studies carried out earlier, is thus confirmed (Table 2) (Abreu et al. 2021).

Zeta potential analysis (ζ)

The electrokinetic stability of a colloidal solution can be determined using the zeta potential (ZP) measurements. The zeta potential value conveys the potential stability of the colloidal system. ZP of nanoparticles with values more than ± 30 mV usually has a high degree of stability.

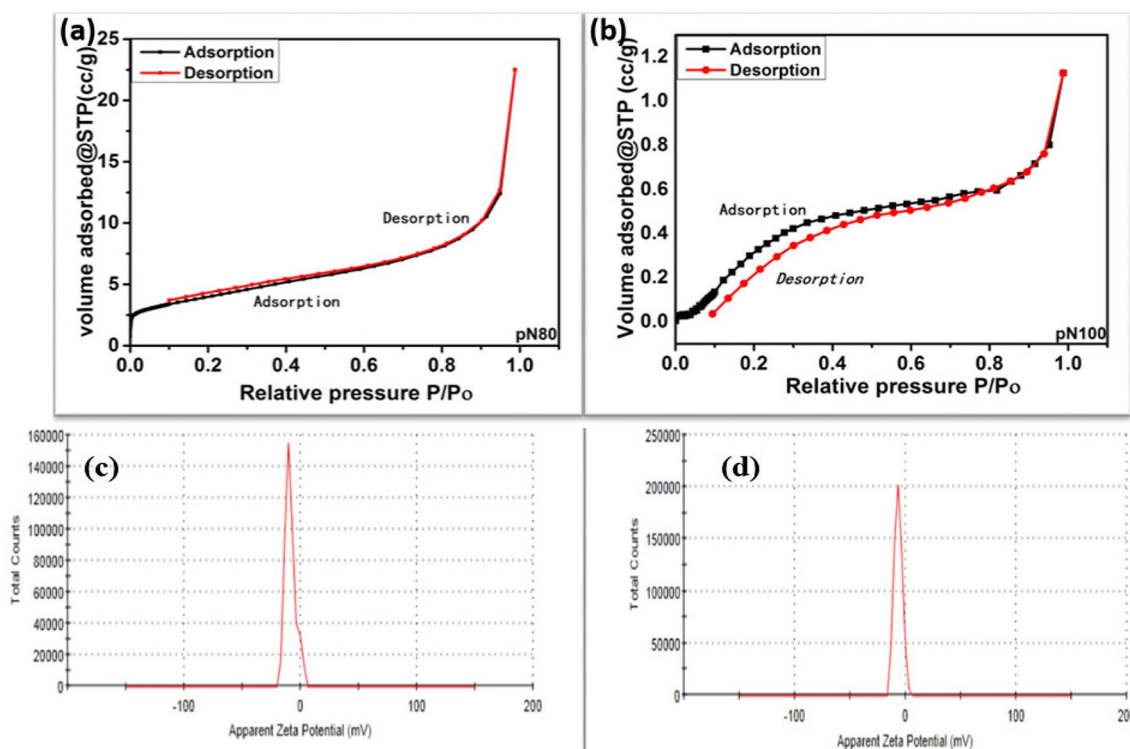


Fig. 5 Nitrogen adsorption–desorption isotherms obtained from the samples: **a** N-80, and **b** N-100. Zeta potential analysis of **c** pN80 and **d** pN100 catalyst

Table 2 Specific surface area and pore volume obtained from BET characterization for pN-80 and pN-100

Parameters	pN-80	pN-100
Specific surface area (m ² /g)	4.047	0.2485
Specific pore volume (cm ³ /g)	0.000092	-0.001127

Table 3 Zeta potential of niobium oxide samples

S. no.	Sample	ζ potential (mV)
1	pN80	-8.83
2	pN100	-6.61

Here, the zeta potential is negative, implying the cumulation of negative charges on the surface of oxide nanoparticles (Behera and Giri 2016; Hossain et al. 2020). The low value of zeta potential represents a flocculated system leading to poor stability. The zeta potential values are tabulated in Table 3, with the medium being water at pH 7. The zeta potential for both the samples is -5mV, indicating them to be in the range of threshold of agglomeration and outside the range of strong/rapid agglomeration and precipitation. Also, for pN80, the zeta potential value is greater than the value of pN100, which implies that the pN80 colloidal solution is well dispersed in the long run when compared to pN100 and has a greater number of accessible active sites on the surface for the redox reaction to occur (Fig. 5c, d). This is due to the electrostatic attraction between the negatively charged catalyst surface and the cationic nature of the methylene blue dye, which has a positive zeta-potential value (Chandrabose et al. 2021).

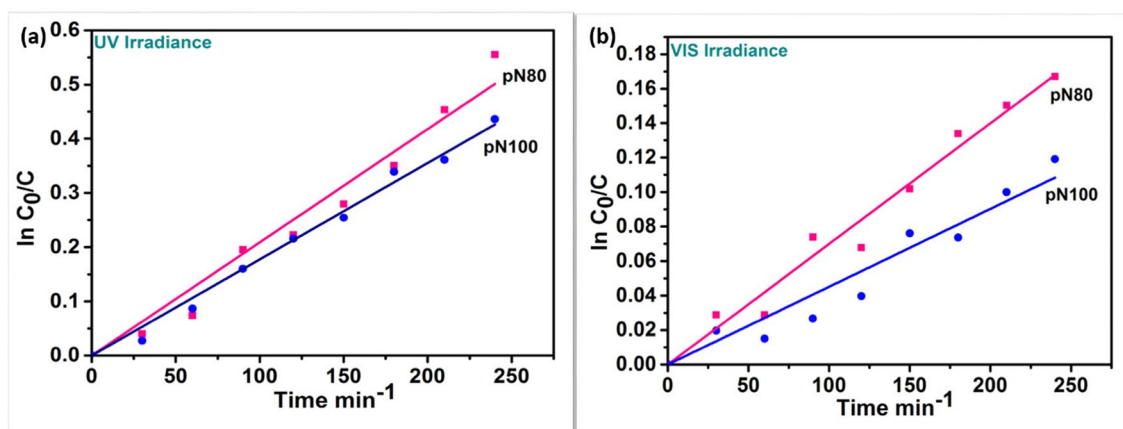
Table 4 Rate constant for both samples under UV and Vis irradiation

Sample	K (UV) min ⁻¹	K(Vis)min ⁻¹	R ²
pN80	0.00209	0.00069	0.991
pN100	0.00178	0.00045	0.992

Photocatalytic studies

The degradation kinetics of pN80 and pN100 catalysts were examined to assess the photocatalytic performance using MB as the probe pollutant under both visible and UV light. Fig. 6a and b present the result of the photocatalytic degradation of MB testing each of the catalysts under UV and visible irradiance, respectively. To estimate the photoactivity of the catalyst, the rate of degradation of dye is predicted by plotting specific concentration vs time under both UV (Fig. 6a) and visible radiation. Figure 8a and b present these plots for the UV and visible radiation, respectively. As depicted in Table 4, the rate constant for the pN80 sample is higher than that of the pN100 sample under both UV and visible illumination. This may be associated with the larger surface area of pN80 nano tripods. The surface area for the pN80 sample is even more than the commercial Nb₂O₅ sample treated at 800°C in the work reported earlier (Van Dijken et al 2000; Kumari et al. 2020). Here, lower-than-expected photoactivity of the pN100 sample may be associated with the sharp reduction in the surface area and the resultant adsorption sites, aggravating the recombination in the crystal structure of pN100 as inferred from the BET and PL results, respectively.

This clearly supports the following correlations: (i) the reaction rate is straightly proportional to the surface area, and (ii) oxygen vacancies created in the crystal lattice

**Fig. 6** Kinetics of photocatalytic degradation for calculation of rate constant of methylene blue dye with Nb-oxide catalyst (a) under UV and (b) under visible irradiance

structure trap the electrons, thereby decreasing its recombination with the holes, and (iii) the nano tripod morphology plays a crucial role in these leading to enhancement in the photocatalytic activity of the sample. As stated earlier, contrary to the expectation here, with an increase in the calcination temperature, the sample pN100 suffered from heavy agglomeration, but the resultant strain led to a decrease in the crystallite size. It resulted in possible blocking of the available pores due to stacking of surfaces one over the other, limiting the active site availability for adsorption of dyes onto the surface. This calls for the need to study adsorption phenomena using both samples.

Adsorption studies

To verify the anomalous behavior during the process of bringing the system to adsorption equilibrium, the adsorption kinetics was investigated. For this, pseudo-first-order and pseudo-second-order models, respectively, were used as given in equations S2 and S3 (Fazal et al. 2019; Chen et al. 2020a, 2020b; Chandrabose et al. 2021). Figure 7 illustrates

the adsorption kinetics of samples. The adsorption percentage calculated using equation S4 in section S9 was found to be 76.05% and 32.7% for pN80 and pN100 catalyst samples, respectively. The maximum adsorption capacity for pN80 was 6.084mg/g and 2.622mg/g for the pN100 sample, respectively, which is also comparable to the experimental value obtained from the graph. Compared to the pseudo-first-order plot, the adsorption data correlated better with the pseudo-second-order reaction as the R^2 value was closer to 1 for the pseudo-second-order reaction (Fazal et al. 2019; Tian et al. 2020). Higher adsorption may be assigned to the increased surface area and comparatively large negative zeta potential value of the pN80 catalyst (Table 5).

Mechanism

A possible photocatalytic mechanism for pN80 nanorods for degradation reaction mechanisms is proposed in Fig 8. The Nb_2O_5 nano-rod/tripods produce electron-hole pairs under both UV and visible irradiation. The electrons get captured in the defects resulting from the oxygen vacancies, which

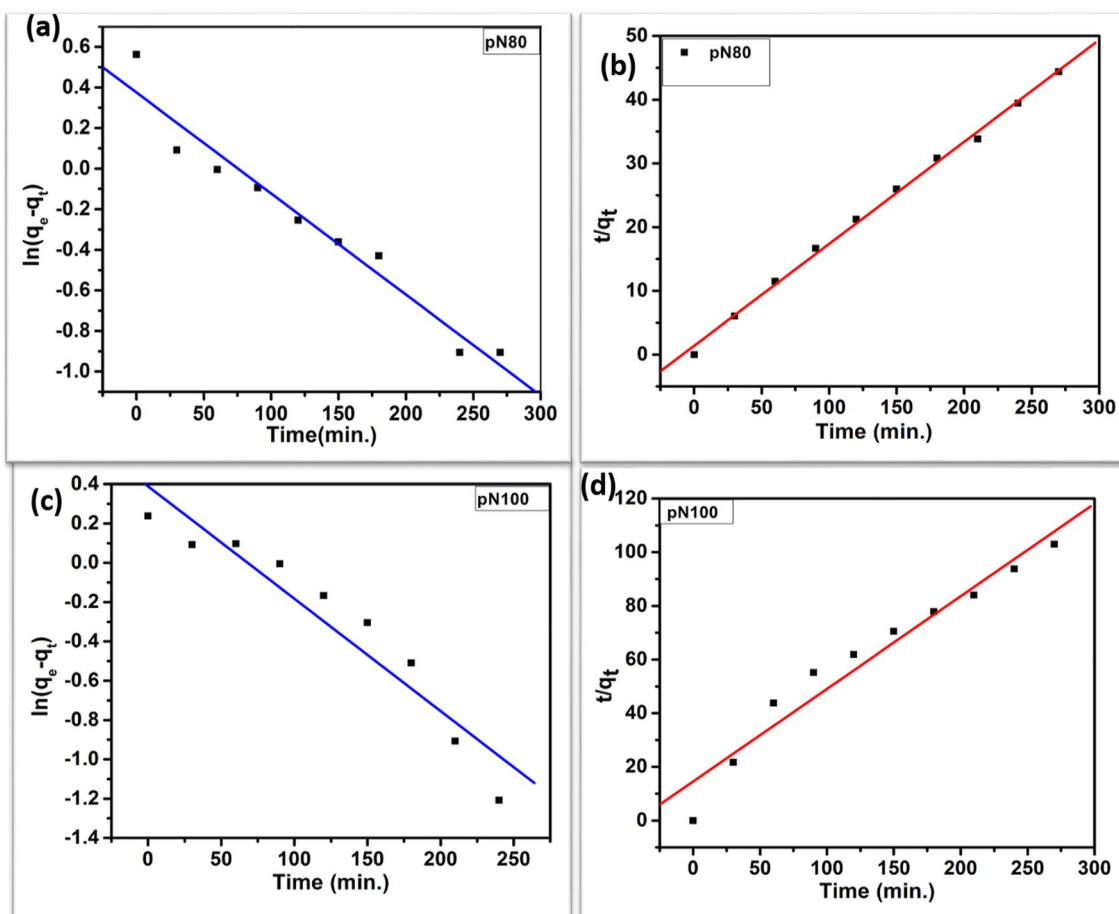
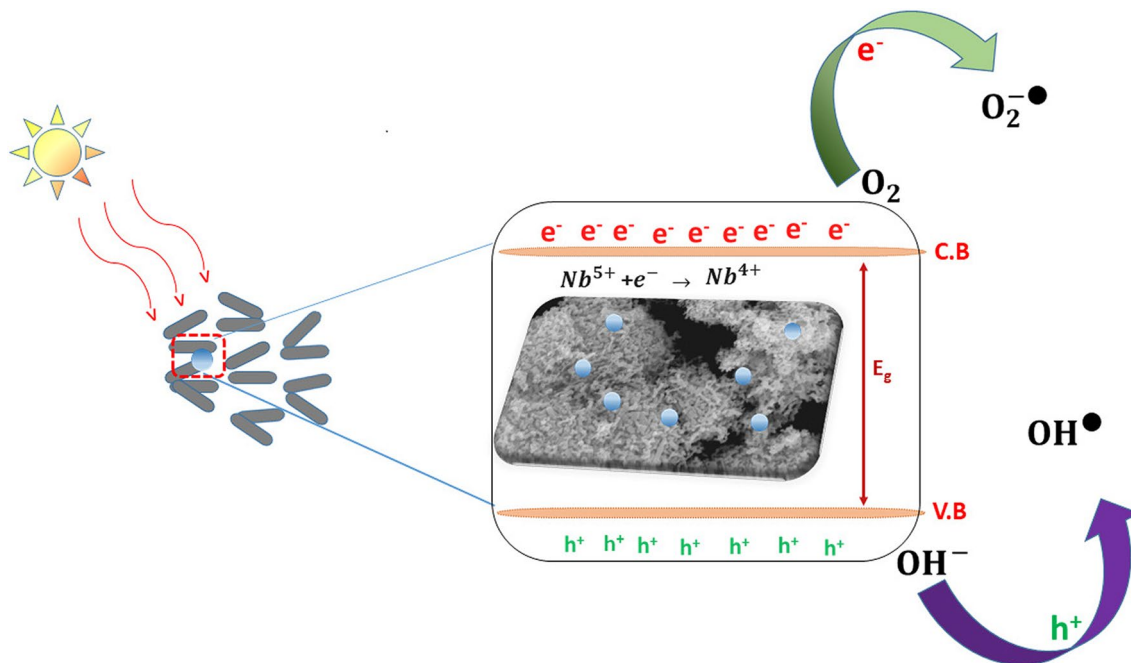


Fig. 7 Adsorption kinetic **a** pseudo-first-order reaction, **b** pseudo-second-order reaction for pN80, **c** pseudo-first-order reaction, **d** pseudo-second-order reaction for pN100

Table 5 Kinetic parameters for pseudo-first-order and pseudo-second-order reaction.

Sample	Pseudo-first-order Kinetics			Pseudo-2nd-order Kinetics		
	q_e (mgg ⁻¹)	K_1 (min ⁻¹)	R^2	q_e (mgg ⁻¹)	K_2 (min ⁻¹)	R^2
pN80	2.731	0.371	0.954	6.25	0.018	0.997
pN100	2.453	0.013	0.909	2.896	0.004	0.948

**Fig. 8** Mechanism of photocatalysis process

depreciate the chances of recombination of the electrons. These electrons are captured by the surface oxygen to form superoxide radicals. The holes, on the other hand, interact with H₂O or OH⁻ to form hydroxyl radicals. These reactive species, in turn, react with dye molecules present in the solution and break them into degraded products. The oxygen vacancies created due to PEI soft template mediated nanostructurization play a vital role. Also, the unique property of niobium pentoxide surface to form unstable hydrocolloids paves the way for the perpetual availability of the active sites.

Conclusion

In summary, the incorporation of PEI as a soft template in the hydrothermal synthesis of niobium pentoxide resulted in orthorhombic and monoclinic phases at calcination temperatures of 800 and 1000°C, respectively. The best adsorption capability and photocatalytic activity are observed for the sample calcined at 800°C, resulting in a degradation efficiency of 98.8% of methylene blue dye in UV and 89.45%

in VIS. For the pN100 sample, the resulting degradation efficiency is 46.05% and 40.35% in UV and VIS, respectively. The enhanced photocatalytic performance of the prepared catalyst is attributable to the formation of a novel ordered nano-rod/tripod structure, the resultant increase in the specific surface area, and the negative zeta potential. These attributes offer a stable hydrocolloid, essential for the efficient and rapid degradation of methylene blue under dark, UV, and visible light conditions.

Supplementary Information The online version contains supplementary material available at <https://doi.org/10.1007/s11356-023-31001-w>.

Author contribution All authors contributed to the study conception and design. Material preparation, data collection, and analysis were performed by Neha Kumari, Sanjoy Kumar Samdarshi, Kumar Gaurav, Arnab S. Bhattacharyya, Ranjana Verma Uday Deshpande, and Kaushtubha Mohanty. The first draft of the manuscript was written by Neha Kumari and all authors commented on previous versions of the manuscript. All authors read and approved the final manuscript.

Funding This study received financial support provided by MHRD, New Delhi, to the Centre for Excellence in Green and Efficient Energy Technology (CoE-GEET). N.K and K G would like to acknowledge Ministry of New and Renewable Energy (Govt. of India) for the support

provided in terms of National Renewable Energy fellowship. NK would also like to acknowledge Material Research Centre, Malaviya National Institute of Technology (MNIT) Jaipur for FESEM and Zeta potential instrumentation facility and SICART Anand, Gujrat for TEM facility and UGC-DAE Consortium for Scientific Research, Indore for XPS facility.

Data availability Will be made available as per request.

Declarations

Ethical approval Not required as no human subjects involved.

Consent to participate Not required as no human subjects involved.

Consent to publish All authors provide their consent to publish this study.

Competing interests The authors declare no competing interests.

References

- Abreu E, Fidelis MZ, Fuziki ME, Malikoski RM, Mastsubara MC, Imada RE, De Tuesta LD, Gomes HT, Anzillero MD, Baldykowski B, Dias DT, Lenzi GG (2021) Effect of thermal treatment on Nb₂O₅ as photocatalyst. *J Photochem Photobiol A Chem* 419:113484–113498
- Alavi SJ, Khalili N, Kazemi R, Verma KD, Darroudi M (2015) Role of polyethyleneimine (PEI) in synthesis of zinc oxide nanoparticles and their cytotoxicity effects. *Ceram Int* 41:10222–10226
- Ancy K, Bindhu MR, Bai JS et al (2022) Photocatalytic degradation of organic synthetic dyes and textile dyeing waste water by Al and Fe co-doped TiO₂ nanoparticles. *Environ Res* 206:112492
- Arcanjo GS, Mouteer AH, Bellato CR et al (2018) Heterogeneous photocatalysis using TiO₂ modified with hydroxalite and iron oxide under UV–visible irradiation for color and toxicity reduction in secondary textile mill effluent. *J Environ Manag* 211:154–163
- Behera M, Giri G (2016) Inquiring the photocatalytic activity of cuprous oxide nanoparticles synthesized by a green route on methylene blue dye. *Int J Ind Chem* 7:157–166
- Boruah B, Gupta R, Modak J, Madras G (2019) Enhanced photocatalysis and bacterio-inhibition in Nb₂O₅ via versatile doping of metal (Sr, Y, Zr, Ag): a critical assessment. *Nanoscale Adv* 1:2748–2760
- Chandrabose G, Dey A, Gaur SS, Pitchaimuthu S, Jagadeesan H, Braithwaite NS, Selvaraj V, Kumar V, Krishnamurthy S (2021) Removal and degradation of mixed dye pollutants by integrated adsorption-photocatalysis technique using 2-D MoS₂/TiO₂ nanocomposite. *Chemosphere* 279:130467–130479
- Chen J, Wang H, Huang G, Zhang Z, Han L, Song W, Li M, Zhang Y (2017) Facile synthesis of urchin-like hierarchical Nb₂O₅ nanospheres with enhanced visible light photocatalytic activity. *J Alloys Compd* 728:19–28
- Chen J, Xiong Y, Duan M, Li X, Li J, Fang S, Qin S, Zhang R (2020a) Insight into the synergistic effect of adsorption – photocatalysis for the removal of organic dye Pollutants by Cr-Doped ZnO. *Langmuir* 36:520–533
- Chen KW, Chen LS, Chen CM (2019) Post-treatment of Nb₂O₅ compact layer in dye-sensitized solar cells for low-level lighting applications. *J Mater Sci Mater Electron* 30:15105–15115
- Chen Y, Xiang Z, Wang D, Kang J, Qi H (2020b) Effective photocatalytic degradation and physical adsorption of methylene blue using cellulose / GO / TiO₂. *RSC Adv* 10:23936–23943
- Cui C, Guo R, Ren E, Xiao H, Lai X, Qin Q (2021) Facile hydrothermal synthesis of rod-like Nb₂O₅ / Nb₂CT x composites for visible-light driven photocatalytic degradation of organic pollutants. *Environ Res* 193:110587–110598
- Dijken AV, Mulenkamp EA, Vanmekelberg D, Meijerink A (2000) The kinetics of radiative and non radiative processes in nanocrystalline ZnO particles upon photoexcitation. *J Phys Chem B* 104:1715–1723
- Dupin J, Gonbeau D, Levasseur A, Cedex P, Cedex T (2000) Systematic XPS studies of metal oxides, hydroxides and peroxides. *Phys Chem Chem Phys* 2:1319–1324
- Ebrahimi A, Jafari N, Ebrahimipour K, Karimi M, Rostamia S, Behnami A et al (2021) A novel ternary heterogeneous TiO₂/BiVO₄/NaY-Zeolite nanocomposite for photocatalytic degradation of microcystin-leucine arginine (MC-LR) under visible light. *Ecotoxicol Environ Saf* 210:111862
- Essawy AA, Sayyah SM, El-nggar AM (2017) Wastewater remediation by TiO₂–impregnated chitosan nano-grafts exhibited dual functionality: high adsorptivity and solar-assisted self-cleaning. *J Photochem Photobiol B Biol* 173:170–180
- Fazal T, Razaq A, Javed F, Hafeez A, Rashid N, Amjad US, Saif M, Rehman U, Faisal A, Rehman F (2019) *J Hazard Mater* 390:121623
- Gupta A, Mittal M, Singh MK, Suib SL (2018) Low temperature synthesis of NbC /C nano-composites as visible light photoactive catalyst. *Sci Rep* 8:1–18
- Hayati P, Mehrabadi Z, Karimi M, Janczak J, Mohammadi K, Mahmoudi G et al (2021) Photocatalytic activity of new nanostructures of an Ag (i) metal–organic framework (Ag-MOF) for the efficient degradation of MCPA and 2, 4-D herbicides under sunlight irradiation. *New J Chem* 45(7):3408–3417
- He J, Hu Y, Wang Z, Lu W, Yang S, Wu G, Wang Y, Wang S, Gu H, Wang J (2014) Hydrothermal growth and optical properties of Nb₂O₅ nanorod arrays. *J Mater Chem C* 2:8185–8190
- Hossain N, Nizamuddin S, Griffin G, Selvakannan P (2020) Synthesis and characterization of rice husk biochar via hydrothermal carbonization for wastewater treatment and biofuel production. *Sci Rep*:1–15. <https://doi.org/10.1038/s41598-020-75936-3>
- Hu Z, He Q, Liu Z, Liu X, Qin M, Wen B, Shi W, Zhao Y, Li Q, Mai L (2020) Stable lithium storage with high areal capacity. *Sci Bull* 65:1154–1162
- Jain M, Seth JR, Hegde LR, Sharma KP (2020) Unprecedented self-assembly in dilute aqueous solution of polyethyleneimine: formation of fibrillar network. *ACS Macromol* 53:8974–8981
- Jian Y, Yu T, Jiang Z, Yu Y, Douthwaite M, Liu J, Albilali R, He C (2019) In-depth understanding of the morphology effect of α-Fe₂O₃ on catalytic ethane destruction. *ACS Appl Mater Interfaces* 11:11369–11383
- Kaciulis S, Mattogno G, Galdikas A, Mironas A, Setkus A (2014) Influence of surface oxygen on chemoresistance of tin oxide film influence of surface oxygen on chemoresistance of tin oxide film. *J Vac Sci Technol A* 3164:14–19
- Karimi-Maleh H, Darabi R, Karimi F, Karaman C, Shahidi SA, Zare N et al (2023) State-of-art advances on removal, degradation and electrochemical monitoring of 4-aminophenol pollutants in real samples: a review. *Environ Res* 222. <https://doi.org/10.1016/j.envres.2023.115338>
- Kong L, Zhang C, Wang J, Qiao W, Ling L (2016) Nano architected Nb₂O₅ hollow, Nb₂O₅ @ carbon and NbO₂ @ carbon core-shell microspheres for ultrahigh-rate intercalation pseudocapacitors. *6*. <https://doi.org/10.1038/srep21177>
- Kulkarni AK, Praveen CS, Sethi YA, Panmand RP, Arbuji SS, Naik SD, Ghule AV, Kale BB (2017) Nanostructured N-doped orthorhombic Nb₂O₅ as an efficient stable photocatalyst for hydrogen generation under visible light. *Dalton Trans* 46:14859–14868

- Kumari N, Gaurav K, Samdarshi SK, Bhattacharya AS, Paul S, Rajbongshi B, Mohanthy K (2020) Dependence of photoactivity of niobium pentoxide (Nb₂O₅) on crystalline phase and electrokinetic potential of the hydrocolloid. *Sol Energy Mater Sol Cells* 208:110408–110417
- Lakhi KS, Park D, Singh G, Talapaneni SN, Ravon U, Bahily KA, Vinu A (2017) Energy efficient synthesis of highly ordered mesoporous carbon nitrides with uniform rods and their superior CO₂ adsorption capacity. *J Mater Chem A* 5:16220–16223
- Lee B, Lu D, Kondo JN, Domen K (2002) Three-dimensionally ordered mesoporous niobium oxide. *J Am Chem Soc* 124:11256–11257
- Li Y, Qin Z, Guo H, Yang H, Zhang G (2014) Low-temperature synthesis of anatase TiO₂ nanoparticles with tunable surface charges for enhancing photocatalytic activity. *PLoS One*:1–19. <https://doi.org/10.1371/journal.pone.0114638>
- Lin X, Wu M, Wang Y et al (2011) Novel counter electrode catalysts of niobium oxides supersede Pt for dyesensitized solar cells. *Chem Commun* 47:11489–11491. <https://doi.org/10.1039/c1cc14973c>
- Liu H, Gao N, Liao M, Fang X (2015) Hexagonal-like Nb₂O₅ nanoplates-based photodetectors and photocatalyst with high performances. *Sci Rep* 5:1–9
- Ma Q, Rosenberg RA (2001) Surface study of niobium samples used in superconducting RF cavity production. *Proc IEEE Part Accel Conf* 2:1050–1052. <https://doi.org/10.1109/pac.2001.986573>
- Ma X, Chen Y, Li H, Cui X, Lin Y (2015) Annealing-free synthesis of carbonaceous Nb₂O₅ microspheres by flame thermal method and enhanced photocatalytic activity for hydrogen evolution. *Mater Res Bull* 66:51–58
- Martín RF, Prietzel C, Koetz J (2021) Template-mediated self-assembly of magnetite-gold nanoparticle superstructures at the water-oil interface of AOT reverse microemulsions. *J Colloid Interface Sci* 581:44–55
- Merino NA, Barbero BP, Eloy P, Cadu LE (2006) La_{1-x}CaxCoO₃ perovskite-type oxides: Identification of the surface oxygen species by XPS. *Appl Surf Sci* 253:1489–1493
- Mohammadi R, Alamgholiloo H, Gholipour B, Rostamnia S, Khaksar S, Farajzadeh M, Shokouhimehr M (2020) Visible-light-driven photocatalytic activity of ZnO/g-C₃N₄ heterojunction for the green synthesis of biologically interest small molecules of thiazolidinones. *J Photochem Photobiol A Chem* 402:112786
- Nowak I, Ziolk M (1999) Niobium compounds: preparation, characterization, and application in heterogeneous catalysis. *Chem Rev* 99:3603–3624
- Pérez-page M, Yu E, Li J, Rahman M, Dryden DM, Vidu R, Stroeve P (2016) Template-based syntheses for shape-controlled nanostructures. *J Colloid Interface Sci* 234:51–79
- Phan CM, Nguyen HM (2017) Role of capping agent in wet synthesis of nanoparticles. *J Phys Chem A* 121:3213–3219
- Poolakkandy RR, Menampambath MM (2020) Soft-template-assisted synthesis: a promising approach for the fabrication of transition metal. *Nanoscale Adv* 2:5015–5045. <https://doi.org/10.1039/d0na00599a>
- Prado AGS, Bolzon LB, Pedrosa CP, Moura AO, Costa LL (2008) Nb₂O₅ as efficient and recyclable photocatalyst for indigo carmine degradation. *Appl Catal B Environ* 82:219–224
- Prieto-Mahaney OO, Murakami N, Abe R, Ohtani B (2009) Correlation between photocatalytic activities and structural and physical properties of titanium(IV) oxide powders. *Chem Lett* 38:238–239
- Raba AM, Bautista-Ruiz J, Joya MR (2016) Synthesis and structural properties of niobium pentoxide powders: a comparative study of the growth process. *Mater Res* 19:1381–1387
- Rueda-Marquez JJ, Levchuk I, Fernández Ibañez P, Sillanpää M (2020) A critical review on application of photocatalysis for toxicity reduction of real wastewaters. *J Clean Prod* 258. <https://doi.org/10.1016/j.jclepro.2020.120694>
- She L, Yan Z, Kang L, He X, Lei Z, Shi F, Xu H (2018) Nb₂O₅ nanoparticles anchored on an n-doped graphene hybrid anode for a sodium-ion capacitor with high energy density. *ACS Omega* 3:15943–15951
- Singh N, Deo MN, Nand M, Jha SN, Roy SB (2016) Materials: oxides, hydrides, and hydrocarbons Raman and photoelectron spectroscopic investigation of high-purity niobium materials: Oxides, hydrides, and hydrocarbons. *Appl Phys* 120:114902–111912
- Souza RP, Freitas TKFS, Domingues FS et al (2016) Photocatalytic activity of TiO₂, ZnO and Nb₂O₅ applied to degradation of textile wastewater. *J Photochem Photobiol A Chem* 329:9–17. <https://doi.org/10.1016/j.jphotochem.2016.06.013>
- Taghavi R, Rostamnia S, Farajzadeh M, Karimi-Maleh H, Wang J, Kim D et al (2022) Magnetite metal-organic frameworks: applications in environmental remediation of heavy metals, organic contaminants, and other pollutants. *Inorg Chem* 61(40):15747–15783
- Tian C, Zhao H, Sun H, Xiao K, Keung P (2020) Enhanced adsorption and photocatalytic activities of ultrathin graphitic carbon nitride nanosheets: kinetics and mechanism. *Chem Eng J* 381:122760–122770
- Tsang E, Zhou X, Ye L, Tsang SCE (2012) Nanostructured Nb₂O₅ catalysts. *Nanotechnol Rev* 3:1–11
- Usha N, Sivakumar R, Sanjeeviraja C, Arivanandhan M (2015) Niobium pentoxide (Nb₂O₅) thin films: rf Power and substrate temperature induced changes in physical properties. *Opt Int J Light Electron Opt*. <https://doi.org/10.1016/j.ijleo.2015.05.036>
- Wang Y, Xin F, Yin X, Song Y, Xiang T, Wang J (2018) Arginine-assisted hydrothermal synthesis of urchin like nb₂o₅ nanostructures composed of nanowires and their application in cyclohexanone ammoxidation. *J Phys Chem C* 122:2155–2164
- Watanabe K, Kuroda K, Nagao D (2021) Polyethylenimine-assisted synthesis of hollow silica spheres without shape deformation. *Mater Chem Phys* 262:124267–124273
- Xie Y, Kocaefe D, Chen C, Kocaefe Y (2016) Review of research on template methods in preparation of nanomaterials. *J Nanomater* 2016
- Yan J, Wu G, Guan N, Li L (2014) Nb₂O₅/TiO₂ heterojunctions: synthesis strategy and photocatalytic activity. *Appl Catal B Environ* 152:280–288
- Zhang Z, Zhang G, He L, Sun L, Jiang X, Yun Z (2014) Synthesis of niobium oxide nanowires by polyethylenimine as template at varying pH values. *Cryst Eng Comm* 16:3478–3482
- Zhao W, Zhu G, Lin T, Xu F, Huang F (2016) Black Nb₂O₅ Nanorods with improved solar absorption and enhanced photocatalytic activity. *Dalton Trans* 45:3888–3894
- Zhu H, Jiang R, Liu L (2013) CdS nanocrystals/TiO₂/crosslinked chitosan composite: facile preparation, characterization and adsorption-photocatalytic properties. *Appl Surf Sci* 273:661–669

Publisher's Note Springer Nature remains neutral with regard to jurisdictional claims in published maps and institutional affiliations.

Springer Nature or its licensor (e.g. a society or other partner) holds exclusive rights to this article under a publishing agreement with the author(s) or other rightsholder(s); author self-archiving of the accepted manuscript version of this article is solely governed by the terms of such publishing agreement and applicable law.